ISSN 1674-1056
http://cpb.iphy.ac.cn
http://iopscience.iop.org/cpb
中国物理 B
Chinese Physics
中国物理 Chinese Physics B

Quantitative HRTEM and its application in the study of oxide materials

Chun-Lin Jia(贾春林), Shao-Bo Mi(米少波), Lei Jin(金磊)
Citation: Chin. Phys. B . 2018, 27(5): 056803. **doi:** 10.1088/1674-1056/27/5/056803

Journal homepage: http://cpb.iphy.ac.cn; http://iopscience.iop.org/cpb

What follows is a list of articles you may be interested in

High-resolution electron microscopy for heterogeneous catalysis research

Yong Zhu(朱勇), Mingquan Xu(许名权), Wu Zhou(周武)
Chin. Phys. B . 2018, 27(5): 056804. **doi:** 10.1088/1674-1056/27/5/056804

Segregations and desorptions of Ge atoms in nanocomposite $Si_{1-x}Ge_x$ films during high-temperature annealing

Yu Wang(汪煜), Meng Yang(杨濛), Gang Wang(王刚), Xiao-Xu Wei(魏晓旭), Jun-Zhuan Wang(王军转), Yun Li(李昀), Ze-Wen Zou(左则文), You-Dou Zheng(郑有炓), Yi Shi(施毅)
Chin. Phys. B . 2017, 26(12): 126801. **doi:** 10.1088/1674-1056/26/12/126801

Structural characteristics of surface-functionalized nitrogen-doped diamond-like carbon films and effective adjustment to cell attachment

Liu Ai-Ping, Liu Min, Yu Jian-Can, Qian Guo-Dong, Tang Wei-Hua
Chin. Phys. B . 2015, 24(5): 056804. **doi:** 10.1088/1674-1056/24/5/056804

Characterization of tetragonal distortion in a thick $Al_{0.2}Ga_{0.8}N$ epilayer with an AlN interlayer by Rutherford backscattering/channeling

Wang Huan, Yao Shu-De
Chin. Phys. B . 2014, 23(9): 096801. **doi:** 10.1088/1674-1056/23/9/096801

Sputtering pressure influence on growth morphology, surface roughness, and electrical resistivity for strong anisotropy beryllium film

Luo Bing-Chi, Li Kai, Kang Xiao-Li, Zhang Ji-Qiang, He Yu-Dan, Luo Jiang-Shan, Wu Wei-Dong, Tang Yong-Jian
Chin. Phys. B . 2014, 23(6): 066804. **doi:** 10.1088/1674-1056/23/6/066804

TOPICAL REVIEW — Electron microscopy methods for the emergent materials and life sciences

Quantitative HRTEM and its application in the study of oxide materials*

Chun-Lin Jia(贾春林)[1,2,3,†], Shao-Bo Mi(米少波)[3], and Lei Jin(金磊)[1]

[1] Ernst Ruska-Centre (ER-C) for Microscopy and Spectroscopy with Electrons, Forschungszentrum Jülich GmbH, 52425 Jülich, Germany
[2] School of Microelectronics, Xi'an Jiaotong University, Xi'an 710049, China
[3] State Key Laboratory for Mechanical Behaviour of Materials, Xi'an Jiaotong University, Xi'an 710049, China

(Received 15 November 2017; revised manuscript received 6 January 2018; published online 26 April 2018)

On the basis of a state-of-the-art aberration-corrected transmission electron microscope, the spherical aberration coefficient C_S of the objective lens can be tuned to either a positive or a negative value. The use of a negative value of C_S combined with an overfocus setting of the objective lens leads to the development of the negative C_S imaging (NCSI) technique. Images obtained using the NCSI technique show superior contrast and signal intensity at atomic column positions than the corresponding positive C_S images, especially for weakly scattering oxygen columns that are in close proximity to strongly scattering cation columns in oxides. Based on the images obtained under the NCSI condition, quantification of the image contrast allows measurements of the atom positions with a precision of a few picometers and the local chemistry on atomic scale. In the present review, we discuss firstly the benefits of the NCSI technique in studies of oxide materials, and then show a procedure for quantitative analysis of the image based on the absolute value of contrast. In the last part, examples are given for the application of the quantitative high-resolution transmission electron microscopy (HRTEM) to the study of electric dipoles of oxide ferroelectrics and atomic-scale chemistry of interfaces.

Keywords: quantitative high-resolution transmission electron microscopy (HRTEM), negative C_S imaging (NCSI), aberration-correction, functional oxides

PACS: 68.37.Og, 68.55.–a, 77.55.fg, 77.80.Dj **DOI:** 10.1088/1674-1056/27/5/056803

1. Introduction

Oxide materials have become increasingly important for electronic applications. In particular, oxide thin films have been the most important material basis for various electronic devices such as non-volatile ferroelectric random-access memory (FRAM) and high density dynamic random access memory (DRAM).[1,2] Lattice defects including interfaces, dislocation and local chemical variation have attracted great attention of research since these defect areas show different electrical properties from the perfect lattice areas.[3–6] These unexpected properties can be considered for application in devices for novel functions.[7] Heterointerfaces and dislocations in oxide systems and domain walls in ferric materials are particularly interesting since these lattice defects can be engineered by the thin film technology[8,9] and their properties and corresponding structure feature can be tested and investigated by various techniques.

Transmission electron microscopy (TEM) has proven to be a powerful tool for materials research. In particular, in the recent decade, great progress in the techniques of high-resolution TEM (HRTEM) has been made by the successful introduction of the spherical aberration (C_S) correctors.[10] Based on the aberration-corrected electron microscope, the point resolution of sub-Å has been achieved.[11] For crystalline materials, the aberration-corrected electron microscopy can be used for determining the position of atomic columns with a precision of a few picometers and the chemical occupancy in atomic columns with a precision of a few atomic percent. With quantitative evaluation of image contrast of a thin crystal, the number of atoms within the atomic columns parallel to the viewing direction has been determined. Up to now, it is possible to characterize the three-dimensional shape of nanoscale crystal with single atom precision.[12]

In comparison with TEM, other structure characterization techniques, such as x-ray and neutron scattering, which are reciprocal-space techniques, provide averaged real-space information from macroscopic areas of material samples. TEM can reveal the structural information from micro-scale to atomic scale. Therefore, TEM and HRTEM are desired techniques for studying the real structural feature at defect-affected areas of matter with sub-Å resolution.

In the present review, we focus our discussion on quantitative HRTEM based on negative C_S imaging (NCSI) technique[13,14] and its applications in studying oxide materials.

*Project supported by the National Natural Science Foundation of China (Grant Nos. 51390472 and 51471169) and the National Basic Research Program of China (Grant No. 2015CB654903).

†Corresponding author. E-mail: c.jia@fz-juelich.de; c.jia@mail.xjtu.edu.cn

© 2018 Chinese Physical Society and IOP Publishing Ltd

2. NCSI technique and benefit to image contrast

In this section, we introduce an imaging technique based on C_S-corrected TEM, the NCSI technique,[13,14] which results in a high-contrast of image in comparison with the conventional positive C_S imaging (PCSI) technique. In order to understand the contrast enhancement under NCSI conditions, an approximation for the object, i.e., weak phase object (WPO), has to be used.

In a very thin specimen, the phase of the propagating electron wave is modified by the object potential. At the exit plane, the wave function $\psi_{EP}(\boldsymbol{r})$ can be written in terms of the specimen potential $U(\boldsymbol{r})$ based on the WPO approximation[14]

$$\psi_{EP}(\boldsymbol{r}) \approx 1 + i\pi\lambda U(\boldsymbol{r})t, \tag{1}$$

where λ is the electron wavelength, $\boldsymbol{r}$ is a vector in the real space and t is the specimen thickness. The wave propagating through the objective lens suffers additional phase shift due to the lens aberrations, among which the spherical aberration coefficient C_S and defocus value Z are two chief parameters. Using different C_S-defocus combinations, we can tune the phase shift of the scattered wave by tuning the aberration function $\chi(\boldsymbol{g}) = \frac{1}{2}Z\lambda\boldsymbol{g}^2 + \frac{1}{4}C_S\lambda^3\boldsymbol{g}^4$, where $\boldsymbol{g}$ is the diffraction vector in the reciprocal space. The classical PCSI condition for optimum phase contrast is obtained by combining a positive value of C_S with an underfocus, which results in a dark-atom contrast. The NCSI condition with a negative value of C_S cooperating with an overfocus leads to a bright-atom contrast.[13]

On the basis of Eq. (1), the contrast enhancement under the NCSI condition can be discussed as follows. At the image plane, the wave function can be written as

$$\psi_{IM}(\boldsymbol{r}) \approx 1 \mp \pi\lambda U(\boldsymbol{r})t, \tag{2}$$

if the objective lens adds a phase of $\pi/2$ or $-\pi/2$ to the diffracted wave, resulting in image intensity recorded in the image plane

$$I(\boldsymbol{r}) = [\psi_{IM}(\boldsymbol{r})]^2 \approx 1 \mp 2\pi\lambda U(\boldsymbol{r})t + [\pi\lambda U(\boldsymbol{r})t]^2, \tag{3}$$

which is correct to the second order in $U(\boldsymbol{r})$. Under the NCSI imaging condition, the sign of the linear term of Eq. (3) is positive and thus the linear and nonlinear terms are additive.[14] In contrast, for the PCSI condition, the sign of the linear term of Eq. (3) is negative and thus the linear and nonlinear terms are subtractive.

Clearly, the contrast modulation due to the projected potential $U(\boldsymbol{r})$ is higher when the linear and nonlinear terms are additive than that when those are abstractive. We should note that this treatment is only valid for very thin specimens. In experiment, the thickness of the used oxide samples (usually include heavy elements) is approximately 2–10 nm, which already exceeds the thickness valid for the WPO approximation. Therefore, a full dynamical calculation of electron scattering and the contrast transfer under partially coherent illumination is required in order to fully investigate the enhancement of the image contrast under the NCSI condition.[15,16]

Figure 1 shows two simulated [110] images of $SrTiO_3$ (STO) under (a) NCSI condition and (b) PCSI condition for a sample thickness of 3.3 nm. The atomic symbols located at atomic column positions demonstrate that the NCSI mode leads to a bright atom contrast under darker background. In contrast, the traditional PCSI mode leads to a dark atomic contrast. The contrasts obtained under the NCSI and PCSI conditions are evidently different, which can be seen by visual inspection of the two images. For quantitative comparison, the image is normalized to an average intensity, so that the standard deviation of the intensity reflects the contrast of the image. For the thickness range of 3.3–6.6 nm, which is most suitable for HRTEM investigations, the image contrast resulting from the NCSI mode is on average by about a factor of 2 larger than the related PCSI contrast.[15]

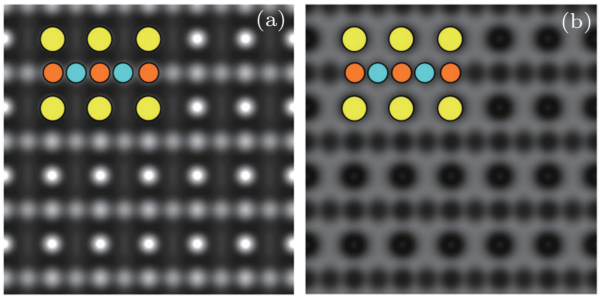


Fig. 1. (color online) Simulated images of STO viewed along the [110] direction under (a) the NCSI condition with $C_S = -15$ μm, defocus $Z = +6$ nm, and (b) the PCSI condition with $C_S = +15$ μm, defocus $Z = -6$ nm for a sample thickness of 3.3 nm. (SrO: yellow, Ti: orange, and O: cyan).[15]

For obtaining reliable results from quantitative HRTEM, a key requirement is the good enough signal intensity of the images, which determines the precision for measurement of the positions and occupancy of the atomic columns in real structure. Figure 2 shows plots of the image intensity profiles for the three types of columns, SrO, Ti and O from the images shown in Fig. 1. The blue line profiles were obtained from the images calculated under the NCSI condition and the red line profiles from the images calculated under the PCSI condition. The mean intensity $I_{mean} = 1$ is denoted by a black line. In comparison with the red line profiles, the blue line profiles show much higher signal intensity at atomic column positions.

Based on the images of the STO crystal shown in Fig. 1, the effects of amorphous layers on the image contrast and thus the measurement precision for atomic positions were investigated.[15] Corresponding to one up to five amorphous layers, random phase object images were added to the calculated STO images in Fig. 1. For each thickness of the amorphous layer, the precision of the position measurement was

quantified by a peak optimization procedure. The results show that the precision obtained under the NCSI condition is by a factor of 2–3 better than that under the PCSI condition (Fig. 7 in Ref. [15]).

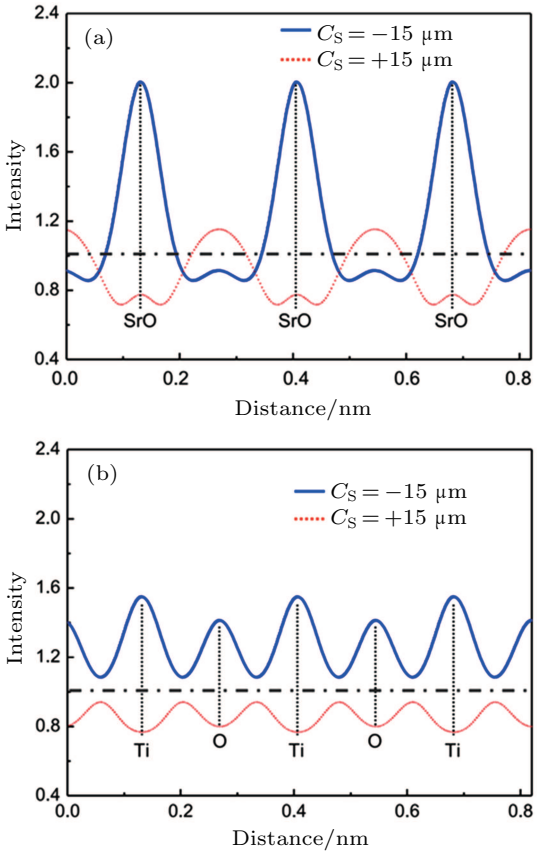


Fig. 2. (color online) Profiles of image intensity for atomic columns of SrO, Ti and O from the NCSI image shown in Fig. 1(a) (blue lines) and from the PCSI image shown in Fig. 1(b) (red lines). Image intensity is normalized to unit mean value.[15]

The dependence of the signal intensity on the atomic number accumulated in individual atomic column was also investigated under both NCSI and PCSI conditions. Along the [110] direction of STO, a unit cell period includes two oxygen atoms in the pure oxygen column, one Ti atom in the Ti column and one Sr atom plus one oxygen atom in the SrO column. Therefore, over a single unit cell period, the sum of atomic numbers in the fully occupied column is 16 (2×8), 22 and 46 (8 + 38) for the oxygen column, the Ti column and the SrO column, respectively. As shown in Fig. 3, under the NCSI condition, the image intensity for all columns follows essentially a linear dependence on the sum of the atomic numbers up to a value of 276. Under the PCSI condition, the linear relation between the intensity and the accumulated atomic number is already lost for all column types at a value of 100. The better linear dependence of the column intensity on the accumulated atomic number under the NCSI condition than that under the PCSI condition benefits measurement of atomic scale chemistry and atom counting in atomic columns.

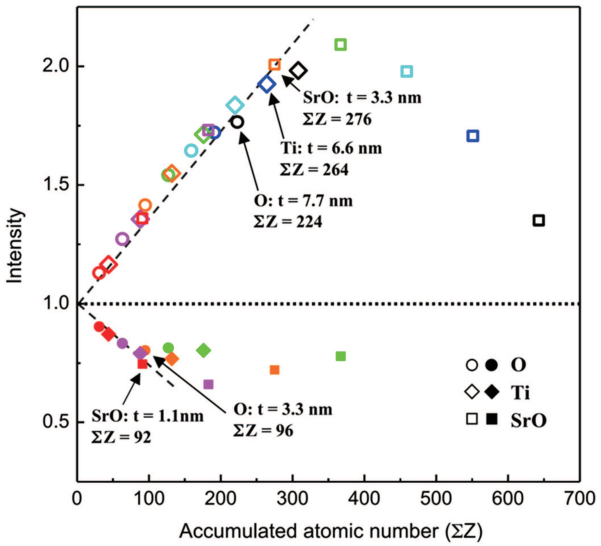


Fig. 3. (color online) Image intensity as a function of the sum of atomic number in atomic columns along the [110] direction of STO for different sample thicknesses under the NCSI condition (solid symbols) and under the PCSI condition (open symbols). The different colors are for different thicknesses of atomic columns.[15]

Based on the image simulations, we have demonstrated that the images obtained under the NCSI condition show great advantages with respect to image contrast, signal intensity for atomic columns, and the linear dependence of the intensity on the atomic number in atom columns. The special features of the negative C_S images are the result of the combining enhancing of the phase contrast with amplitude contrast.[15,16] Therefore, the NCSI technique provides optimum HRTEM condition for direct atomic imaging of material structures, which is the basis for quantitative determination of atomic structures by aberration-corrected TEM.

3. Iterative procedure for quantitative HRTEM based on NCSI

Based on the above results and discussion, under the NCSI conditions, the positions of the image intensity maxima represent already quite well the actual positions of atomic columns. Likewise, for a thin specimen, the height of the intensity maxima is roughly proportional to the accumulated atomic charge number along an atomic column. However, it should be noted that in experiment, residual lens aberrations and small tilts of the specimen orientation away from the fully symmetric Laue orientation are unavoidable and thus affect the contrast of atomic-resolution images, i.e., the positions and image intensity maxima. This means that the images recorded in the microscope include not only the structure information, but also artifacts induced by the deviation from the ideal imaging conditions. In addition, a linear relationship between the observed peak intensity and the actual atomic column occupation is not guaranteed due to the nonlinear nature of electron diffraction. Therefore, in most cases, the data measured directly from an HRTEM image cannot simply be used as the

real atomic feature for interpretation of various properties of materials. Comparison between the experimental image and the simulated one is the most accurate route for removing these artefacts and thus precisely determining the structure of materials at atomic scale.

In practice, an iterative procedure for image comparison is used, as schematically shown in Fig. 4, for determining the true atomic structure of crystals. In this procedure, a structure model for the image area is proposed according to the positions of intensity peaks determined by fitting a two-dimensional Gaussian function to the intensity distribution around the peaks. Based on the structural model, HRTEM images are simulated taking the imaging parameters and some sample parameters (e.g., thickness and crystal tilt) as input variables. The imaging parameters can be estimated and optimized by means of evaluating the azimuth tableau of an amorphous area close to the interesting area of the sample before the atomic resolution images are recorded. For the NCSI condition with a resolution of 0.08 nm (FEI Titan microscope), the images are recorded using a defocus value $\Delta f = 2$–6 nm with the residual lens aberrations $C_S = -13$ μm, two-fold astigmatism $A_2 < 2$ nm, three-fold astigmatism $A_3 < 20$ nm and axial coma $B_2 < 20$ nm.

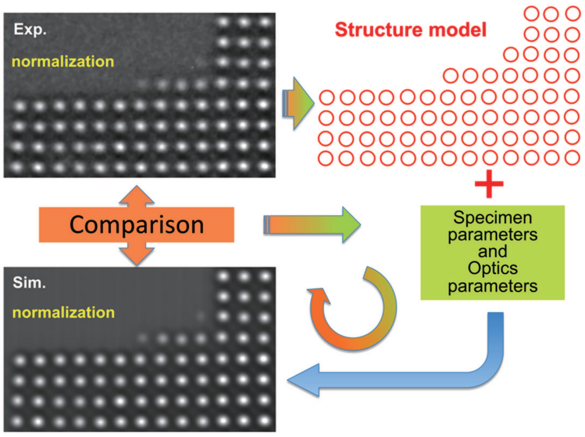


Fig. 4. (color online) Schematic of an iterative procedure for quantitative comparison between experimental and simulated images for determining the true atomic structure of material.[12]

An additional problem is the frequently observed systematic mismatch of the magnitude of the image contrast between simulation and experiment, which was proposed firstly by Hÿtch and Stobbs.[17] For solving this so-called Stobbs-factor problem, in image simulation, the other effective factors dampening image contrast also need to be taken into account, e.g., the modulation transfer function (MTF) of the used charge-coupled-device (CCD) camera[18] and additional image contrast spread function.[12,19] With considering all these effects, HRTEM images are simulated and compared with the experimental image in an iterative way so that the best match between the simulated and experimental images is obtained. Only in the case of the best fit between the experimental and the simulated images with respect to positions and the intensity values of the intensity peaks as well as the true value of the image contrast, one can conclude that the structure model underlying the simulation represents indeed the actual atomic structure.

An excellent example for quantitative HRTEM is the work on determination of three-dimensional shape of MgO nanoscale crystal with atomic resolution.[12] In the work, a complete quantification of experimental and simulated images was performed with an accurate calibration of the relationship between a given atom column and the resulting image intensity. Figure 5(a) shows an atomic-resolution image of a MgO single crystal specimen containing side terraces parallel to viewing direction (edge of image). The image was recorded along the [100] direction of MgO using the NCSI technique. Under the NCSI conditions and at the particular specimen thickness under investigation, the atom columns, which include the Mg and O atoms that stack alternately along the [100] direction, appear bright under a dark background. A remarkable feature observed in the original image is the sharp image dots, amorphous-free and low noise.

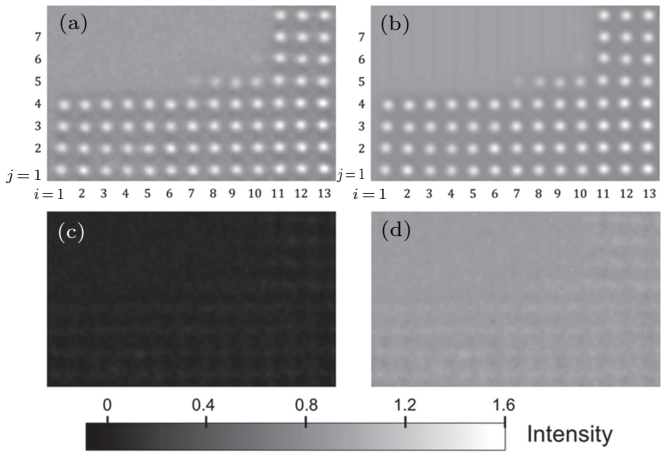


Fig. 5. Comparison of true contrast between the experimental (a) and the best fitting simulated (b) images of MgO. *i* and *j* index the intensity maxima, which were quantified with respect to the absolute intensity and geometric position. (c) The difference image between the experimental (a) and the best fitting simulated (b) images. (d) The difference image with enhanced intensity by adding the value of the mean intensity of the normalized simulated image. Note that all of the images are displayed with the same intensity scale.[12]

Figure 5(b) displays the simulated image with the best match to the experimentally observed image of Fig. 5(a), which was obtained employing the iterative comparison procedure. Figure 5(c) shows the difference image between the experimental and the best match simulated images. The three images are all displayed with the same intensity scale. The difference image shows a very low intensity and contrast, indicating the excellent fit between the simulated and the experimental images. In order to show the contrast details of the difference image, the intensity of the difference image shown

in Fig. 5(d) is artificially enhanced by adding intensity mean of the normalized simulated image. Figure 6(a) shows a quantitative comparison of the peak intensity values at the atomic columns measured directly from the experimental image (solid circles) with those of the best fitting simulated image (open squares). The visible discrepancy in some of the circle-square pairs corresponds to an intensity level of image noise in vacuum. Figure 6(b) plots the difference ($\delta_{\rm Pos}$) in positions (x, y) of the intensity maxima between the experimental and simulated images. The standard deviation for the position fitting is 0.5 pm for both x and y coordinates. Based on the data of quantitative comparison, the excellent reproduction of the experimental data by the best fitting simulation indicates that the simulation parameters, including specimen thickness, specimen tilt, absorption and optical aberrations, have been determined with a sufficiently high accuracy to establish a reliable basis for the precise quantification of the atomic structure of the crystal.

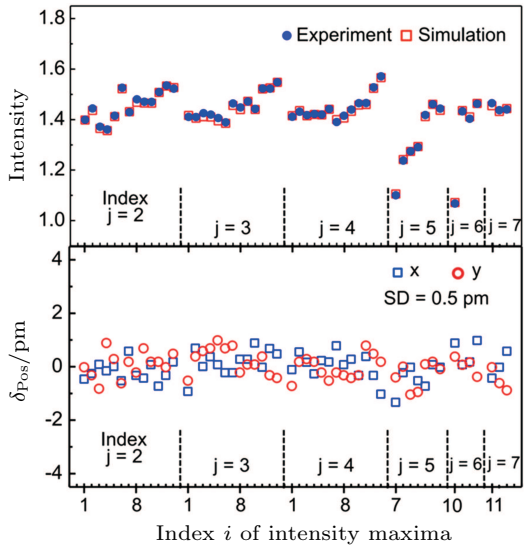


Fig. 6. (color online) (a) Comparison of the data derived directly from the experimental image shown in Fig. 5(a) (solid circles) with those derived from the best fitting simulated image shown in Fig. 5(b) (open squares) for the peak intensity at atomic positions. (b) The difference $\delta_{\rm Pos}$ in positions of the intensity maxima between the experimental and the simulated images for x (squares) and y (circles) directions. The standard deviation (SD) for the position difference is 0.5 pm for both x and y directions. The indexes i, j of the intensity maxima are referred to those in Fig. 5.[12]

In the following, examples are presented for the application of the quantitative HRTEM based on the NCSI technique to characterization of atomic structure and properties of oxides.

4. Atomic-scale study of electric dipoles across domain walls

The physical properties and structures of domain walls in ferroelectrics and multiferroics have been studied theoretically and experimentally.[20–27] It was found that the domain walls possess different properties depending on the atomic details of the walls. The novel properties at domain walls stimulate great interest in experimentally exploring the structure of domain walls at atomic scale.

4.1. Domain walls in ferroelectric $PbZr_{0.2}Ti_{0.8}O_3$ films

Figure 7(a) shows the cubic structure of paraelectric $PbZr_{0.2}Ti_{0.8}O_3$ (PZT) at high temperature. The atomic arrangement in the cubic cell shows a centrosymmetry. The charge centers of anions and cations coincide and just compensate. Upon cooling, the structure becomes tetragonal (Fig. 7(b)) and the material becomes ferroelectric at about 500 °C. Inside the unit cell, the atoms shift to new positions and the centrosymmetry is lost. In particular, the positive and negative charge centers no longer coincide. As a consequence, an electric dipole is formed, resulting in a spontaneous polarization ($\boldsymbol{P}_{\rm S}$, pointing from net negative to net positive charge). In the high-temperature cubic structure, there are six equivalent ⟨100⟩ directions that can be chosen as directions of spontaneous polarization direction. This means that six types of spontaneous polarization domains are possible. In general case, a multi-domain structure is formed in bulk material as shown in Fig. 7(c). Some of the domains are separated by the walls where the polarization vector turns by about 90°. There is another family of walls where the polarization vector changes by 180°. These 180° domain walls can occur in two forms: longitudinal domain wall (LDW), where the dipole vectors have head to head or tail to tail orientation and transversal domain wall (TDW), where the dipoles show head to tail orientation.

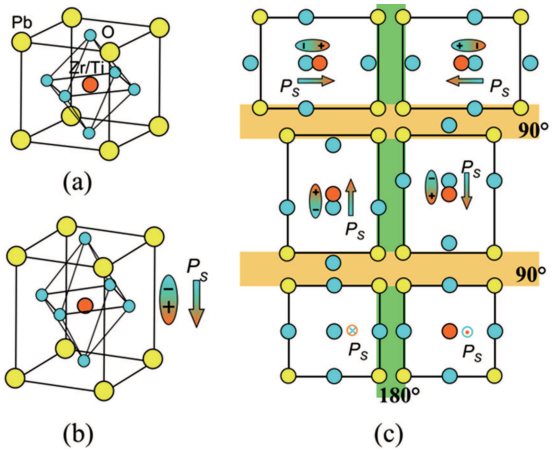


Fig. 7. (color online) (a) The cubic structure of paraelectric PZT at high temperature. (b) The tetragonal structure of ferroelectric PZT. (c) Six possible domains and relative domain walls.

Figure 8 shows an HRTEM image of a 10 nm thick PZT layer between two $SrTiO_3$ layers prepared by pulsed laser deposition.[28,29] The image was recorded along the crystallographic [$\bar{1}$10] direction under the NCSI condition. The insets show magnifications of two areas in the upper left, domain I and the lower right side of the figure, domain II. In

the inserts, yellow circles denote PbO atom columns, red circles the Zr/Ti columns and blue circles the oxygen columns. It can be clearly seen from the inserts that in domain I, the O columns are shifted upward with respect to the neighboring Zr/Ti columns, while in domain II, the shifts of the oxygen columns are in the opposite direction. The relative displacements of the atoms lead to a separation of the center of the anionic negative charge of oxygen from that of the cationic positive charge of the metal cations, resulting in spontaneous polarization $\boldsymbol{P}_S$ as indicated by color arrows. In fact, the image of Fig. 8 contains two 180° polarization domains. The position of the respective 180° domain wall is denoted by a dotted line, which was determined directly by mapping the atomic displacements.

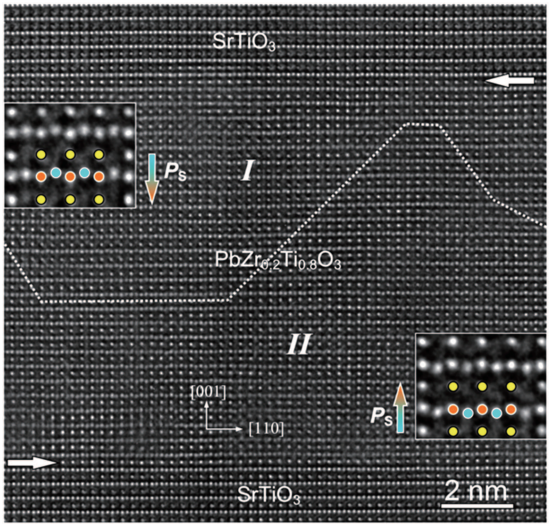


Fig. 8. (color online) Atomic-scale image of a STO/PZT/STO thin-film heterostructure, recorded along the [$\bar{1}$10] direction under the NCSI condition. The horizontal arrows denote the horizontal interfaces between the PZT and the top and the bottom STO film layers. The dotted line traces the 180° domain wall. The arrows of $\boldsymbol{P}_S$ show the directions of the polarization. Insets display magnifications of the dipoles formed by the displacements of ions in the unit cells (yellow: PbO, red: Zr/Ti, blue: O).[29]

We are particularly interested in the part of domain wall on the left side of Fig. 8, the part of LDW. This part of domain wall is enlarged and displayed in Fig. 9(a). The arrows indicate the geometrical center of the domain wall. We quantified the image area and determined the atom positions using the above-described iterative procedure. Based on the quantitatively determined positions, the c- and a-axis lattice parameters as well as the displacements of the Zr/Ti atomic columns $\delta_{Zr/Ti}$ and O atom columns δ_O were calculated. Since we are only interested in the behavior of these parameters as a function of distance from the domain wall center, we calculated a mean value for a given distance from the central plane by averaging the position data parallel to the domain wall over the horizontal width of Fig. 9(a).

In Fig. 9(b), blue squares and red circles denote the off-center displacements along the [001] direction of the O columns and the Zr/Ti columns, respectively, as a function of the vertical separation from the domain wall plane. Figure 9(c) shows the spontaneous polarization versus distance from the central plane of the domain wall. The values of $\boldsymbol{P}_S$ are calculated on the basis of the c-axis lattice parameters and the atomic displacements shown in Fig. 10(a) and the effective charge values of the ions for $PbTiO_3$. The maximum value of the modulus of $\boldsymbol{P}_S$ is about 75 μC/cm^2 for domain I and about 80 μC/cm^2 for domain II. Inside the domain wall, the polarization reaches zero at the wall center plane and changes direction across the plane.

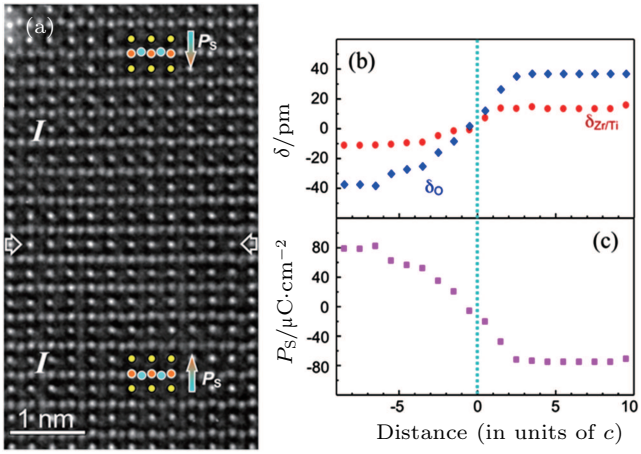


Fig. 9. (color online) (a) Image of an LDW segment. Arrows denote the geometric central plane of the domain wall, which is referred to as the origin for quantitative analysis of the dipole distortion across the domain wall area. (b) The displacements of the Zr/Ti atoms ($\delta_{Zr/Ti}$) and the O atoms (δ_O) across the LDW. Positive values denote upward shifts and negative values downward shifts. (c) The spontaneous polarization $\boldsymbol{P}_S$. The positive values represent upward polarization and the negative values downward polarization.[29]

Figure 10(a) shows an atomic resolution image of an area including the interface between the PZT layer and the STO substrate,[23] recorded along the [110] direction. In the image, the projected unit cell of PZT is schematically indicated in three regions with red circle for the Zr/Ti column, yellow for the PbO column and blue for the O column. For the sample thickness of about 11 nm, dynamic electron scattering yields a sharp bright contrast for the Zr/Ti and the O atom columns, while the PbO atomic columns are relatively weak. The film–substrate interface was marked by depositing a nominally 1.5 unit cells thick layer of $SrRuO_3$ (SRO) on STO prior to the deposition of PZT. The interface, denoted by a horizontal dashed line, is then determined by observing the plane of RuO_2 serving as a marker.

In the image of Fig. 10(a), the vertical shift of the Zr/Ti positions is clearly visible with respect to the adjacent O positions, indicating a polarized state. In the left-hand part of the image, this shift is upward; while in the right-hand part, it is downward, resulting in the polarization directions indicated by the arrows. The opposite directions of the two domains form

a 180° domain wall. The position of the domain wall is localized by mapping the atom shifts unit cell by unit cell. At the bottom part of the domain wall, in-plane displacements of the Zr/Ti positions with respect to the adjacent oxygen positions are observed between the two 180° domains.

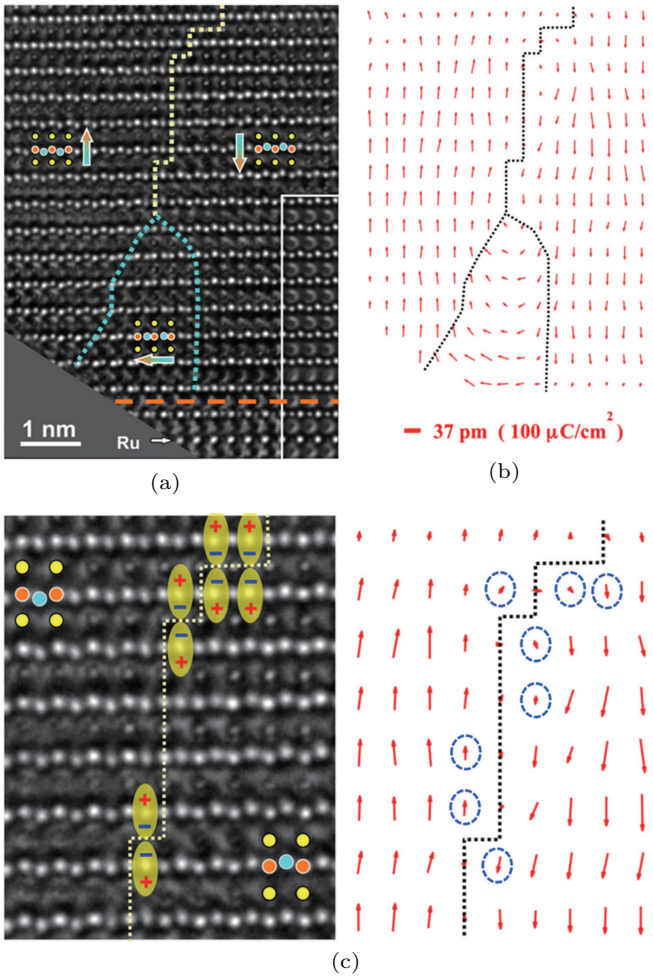


Fig. 10. (color online) (a) Atomic-resolution image of the 180° domain structure in a PZT film close to the interface to the STO substrate, recorded along the [110] direction. The interface is marked by a horizontal dashed line. The domain wall is indicated by a yellow dotted line and the polarization is denoted by arrows. In the center of the lower half of the image, a dotted blue line surrounds an area, where in the center, the polarization direction makes an angle of 90° with the two large domains. The inset on the right-hand side shows a calculated image demonstrating the excellent match to the experimental image. (b) Map of the displacement vectors for the Zr/Ti atoms (arrows) from the center of the projected oxygen octahedra. The arrows represent electric dipole moment of unit cell. Note that the continuous rotation of the dipole directions from "down" (right) to "up" (left) closes the electric flux of the two 180° domains. (c) Magnification of upper part of (a) and (b), showing details of the domain wall facets where polarization charges depolarize the nearby unit cells and reduce the off-center displacements of the atoms in these unit cells.[23]

The off-center displacements of the atoms were quantified by the iterative procedure based on the image in Fig. 10(a). Figure 10(b) displays a vector map of the atomic displacements. In this map, the middle of arrows is located at the Zr/Ti column positions. The arrows indicate the modulus and the direction of the off-center displacement with respect to the middle point of the horizontal line connecting the two neighboring O atom positions. The scale at the bottom left indicates a displacement of 40 pm. We note that a uniform atomic shift of this magnitude corresponds to an integral polarization of 108 μC/cm^2. Considering the proportional relation between the off-center displacement and the electrical dipole moment, the displacement map provides direct evidence of a continuous rotation of the dipole direction from downward in the right-hand domain through a 90° orientation to upward in the left-hand domain, forming a particular type of flux-closure structure.

We note also facets in the upper part 180° domain wall, which is reproduced at larger magnification in Fig. 10(c). In the unit cells at the domain wall plane, the off-center displacements are essentially zero. We find also some displacement vectors, which have significantly reduced modulus as denoted by blue circles. These reduced displacements occur only in the unit cells close to the facets. This phenomenon provides evidence for the effects of the local depolarization field created by the charged facets. In contrast to the LDW in Fig. 8, where the dipoles form a configuration of head-to-head, a tail-to-tail dipole configuration is seen in the facets. The local charges at the facets depolarize the nearby unit cells and thus reduce the off-center displacements of the atoms in these unit cells as measured from the images.

4.2. Domain walls in multiferroic $BiFeO_3$ crystal

$BiFeO_3$ (BFO) is a room-temperature multiferroic that simultaneously displays ferroelectric and antiferromagnetic properties. BFO has a rhombohedral structure with *R*3*c* space group. It can be derived from the perovskite structure by applying a tensile distortion along the direction of a body diagonal ⟨111⟩ in the pseudocubic notation used here. Along this axis, corner-sharing oxygen octahedra rotate around it in an alternating sense. The cations are displaced from their centrosymmetric positions along [111], inducing spontaneous ferroelectric polarization. In addition, BFO exhibits G-type antiferromagnetic ordering, which is considered to relate to the rotation of the oxygen octahedra. Figure 11 shows a perovskite unit cell of pseudocubic structure in (a), and the projected structure along the [110] direction in (b). From the [110] projected structure, the projected off-center displacement Δ and the projected rotation angle α of the oxygen octahedra can be measured.[30]

Figure 12(a) shows an atomic-resolution image of a domain structure viewed along the ⟨110⟩ direction, including three domains labelled D1, D2 and D3. The three domains are separated by domain walls DW1, DW2 and DW3, respectively. In this projection, only the [001] component of the [111] polarization vector can be measured.[30] The domains can be distinguished by checking the off-center displacement of atoms

in each unit cell. Domains D1 and D3 exhibit the same projected structure. In the magnified images (Figs. 12(b)–12(d)), the projected structure along the ⟨110⟩ direction is indicated. Under the NCSI condition and for the approximately 5 nm thick sample, strong contrast is observed for the Fe and the O atom positions, while that of BiO is weak. The O positions in the images are shifted upward and downward, corresponding to the alternating octahedral rotation. The off-center displacement of Fe with respect to the middle point of the line connecting two neighboring O atom positions is clearly visible. This displacement is upward in domains D1 and D3 (Fig. 12(b)) and downward in domain D2 (Fig. 12(c)). As a result of the octahedral rotation and Fe displacement, the chain –O–Fe–O–Fe–O– forms an "arc" inside the projected unit cell. The arc curvature is negative in D1 and D3 and positive in D2. In the wall area DW3 (Fig. 12(d)), the –O–Fe–O–Fe–O– atom positions follow a zigzag line, preserving the rotation of the octahedral, while the off-center displacements of Fe are not seen.

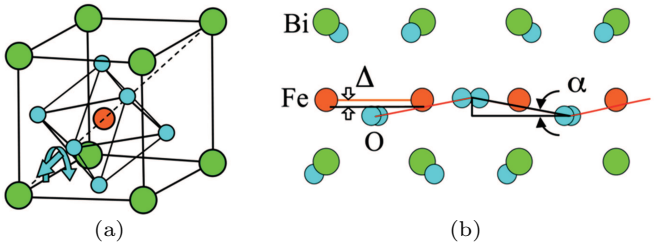


Fig. 11. (color online) (a) Perovskite unit cell of pseudocubic structure of BFO. (b) Projected structure along the [110] direction of the pseudocubic structure.[30]

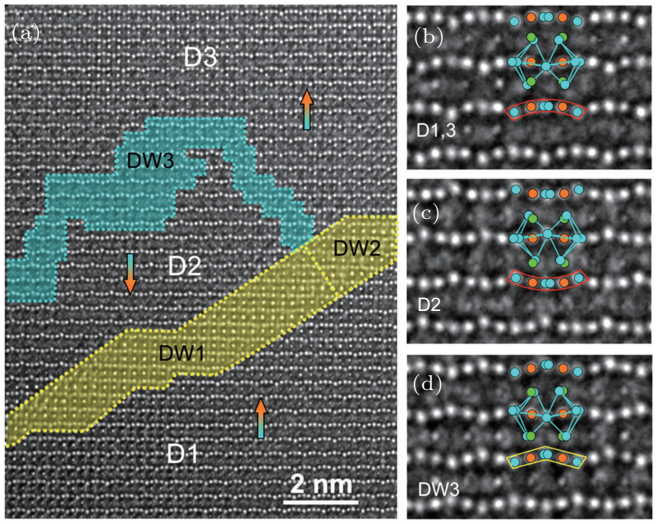


Fig. 12. (color online) (a) Atomic resolution image of domains and domain walls in BFO crystal recorded parallel to the ⟨110⟩ direction. A stripe-domain wall outlined by yellow area consists of two segments, DW1 between domain D1 and domains D2, and DW2 between domain D1 and domain D3. Another domain wall DW3 (blue area) separates domain D2 from D3. Vertical arrows denote the direction of the ⟨001⟩ component of the ⟨111⟩ type polarization vector. Magnified image of the atom arrangement in (b) domains D1 and D3, (c) domain D2, and (d) domain wall area DW3.[30]

The off-center displacements of the Fe atoms and the rotation angles of the O octahedra were studied quantitatively for DW3 and the adjoining domains D2 and D3. In measurement of the displacements of the Fe atoms and the rotation angles of the oxygen octahedra, the effects of residual lens aberrations and unavoidable small tilt of the crystal have been removed in the iterative procedure for quantitative comparison between experimental and simulated images. Figure 13(a) shows a map of the Fe displacements projected into the (110) plane. Arrows centerd at the Fe positions indicate the magnitude and the direction of the displacement. Inside the domains, the mean value of the displacement component is about 17 pm, which is in good agreement with the value of 18 pm derived from the crystallographic model of BFO.[31] In the domain-wall area DW3 (red arrows in the blue area), the displacement changes to the low but finite value of 6 pm. A striking feature in Fig. 13(a) is the high degree of displacement disorder on the atomic scale. Both the magnitude and the direction of the projected displacement vector exhibit substantial random deviations from the exact [001] direction. In some areas, nanometer-scale regions with essentially identical directions of dipole vectors can be recognized (red ellipses) showing large deviations (up to a few tens of degrees) from [001].

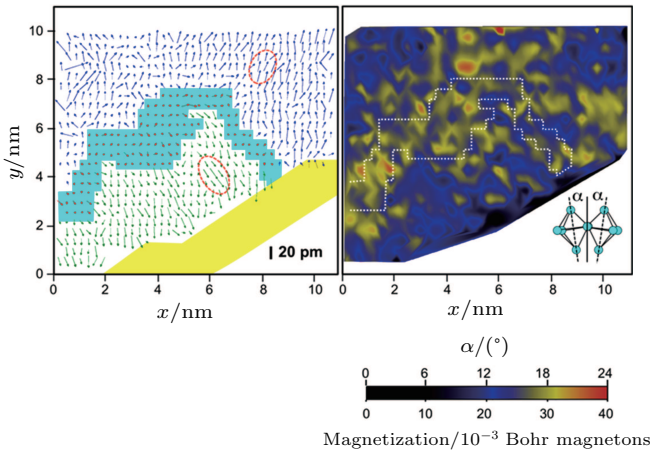


Fig. 13. (color online) (a) Map of the off-center displacements of Fe atom positions in domains D2 (green arrows) and D3 (blue arrows) and in the domain wall area DW3 (red arrows in blue area) projected onto the {110} plane. (b) Map of the magnitude of the oxygen octahedron rotation angle, α, projected into the {110} plane. The area of DW3 is indicated by a white dotted line. A color scale denotes the tilting angles of oxygen octahedra and the magnitude of magnetization.[30]

Recent investigation of dipole configurations in proper ferroelectrics ($BaTiO_3$) by theoretical calculations showed that nontrivial configurations of dipoles could be stabilized by a new mechanism of topological protection, the finite-temperature fluctuations of local dipoles.[32] It was pointed that in order to classify topological defects, one need to explore the topology of full manifold of internal states, that would involve all values of accessible dipoles, in contrast to

the local dipoles that are limited by the symmetry-allowed lattice directions. The important results of the work are the sufficiently high thermal entropy, which allows the local dipoles to significantly deviate from orientations defined by the symmetry allowance. Our experimental observations show indeed the nontrivial configuration of the local dipoles that deviate significantly from the [111] direction in the BFO crystal.

Figure 13(b) shows the magnitude of the octahedron rotation angle in color-coded form. We find that the disorder in the form of fluctuations of the rotation angle extends over the whole image, i.e., both the domain area and the domain-wall area are affected. For the rotation angle projected into the {110} plane, we obtain a mean value of $12.8^\circ \pm 0.14^\circ$ by averaging over the yellow-dominated area, and $10.7^\circ \pm 0.20^\circ$ over the blue-dominated areas. Considering the linear relation between the tilting angles of the oxygen octahedra and the magnetization given in Ref. [33] the map in Fig. 13(b) also demonstrates changes of the unit cell magnetization from area to area.

5. The structure and chemistry across a single-unit-cell layer of $LaAlO_3$ embedded in $SrTiO_3$

Novel functional properties of the interface between insulating $LaAlO_3$ (LAO) and STO have been measured, including metallic conductivity, superconductivity and magnetism. These physical phenomena, which are not intrinsic to the bulk material, can be related to the local atomic rearrangements at the interface, the special feature of the oxide structure, and the strong correlation of electrons to the ionic lattices. For a comprehensive understanding of the origin of these novel properties, subtle details of the atomic structure at the interface area must be taken into account. A simultaneously quantitative determination of the structural and the chemical details at an identical specimen area has become great challenge of transmission electron microscopy. By means of quantitative HRTEM, which is described in Section 3, the chemistry and structure were investigated on atomic scale near a nominally single-unit-cell layer of LAO, which is sandwiched between a capping STO layer and the STO substrate.[19]

Figure 14(a) shows an atomically resolved cross-sectional image of a sample containing nominally a single-unit-cell layer of LAO (blue arrow) sandwiched between a capping layer of STO and the STO substrate. As shown in the simulated image (Fig. 14(c)), under the NCSI condition and at the particular specimen thickness of about 4 nm, one obtains a bright contrast for all atom columns, including the oxygen columns. While the contrast of the Ti and the SrO atom columns is relatively strong, the contrast for the LaO atomic columns is comparatively weaker at a similar level as that of the oxygen columns. Figure 14(b) shows an averaged image over the experimental image area of Fig. 14(a), demonstrating the best match to the simulated image (Fig. 14(c)). The atomic displacements and the chemical intermixing across the nominally single LAO unit cell are iteratively determined by a comparison of the position and the height of the intensity maxima between experimental with corresponding image simulations.

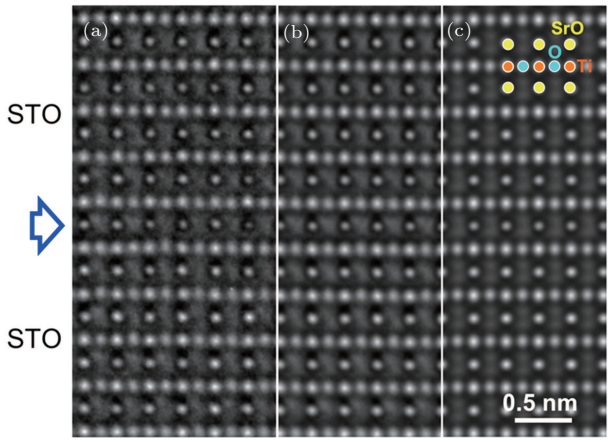


Fig. 14. (color online) (a) Atomic-resolution image of the nominally single unit cell layer of LAO embedded in STO, which was recorded along the [110] direction of STO under the NCSI condition. (b) The averaged image over the image area of (a). (c) Simulated image with the best match to the experimental image. The arrow denotes the nominally single LaO plane.[19]

The final data are displayed in Fig. 15. As shown in Fig. 15(a), the *A*O-type columns, i.e., SrO and LaO, do not show evident shifts across the single unit cell layer. In contrast, shifts of the oxygen columns are measured in the BO_2 plane (*B* represents Ti in STO and Al in LAO). The positive values denote the upward shifts and the negative ones the downward shifts with respect to the *B*-type columns (referring to the image of Fig. 14). On the left (corresponding to above the nominal LaO plane in the image), the shifts are downward, and on the right (below the nominal LaO plane in the image), they are upward. All shifts point towards the nominal LaO plane. The collective displacement of the oxygen atoms leads to a shift of the oxygen octahedron centers away from the *B*-type columns, implying a separation of the center of negatively charged oxygen from the positive charge center of the cations and thus an electric polarization. Figure 14(b) shows concentration profiles across the nominal LaO plane, which was directly obtained from the final structure model determined by the iterative refinement procedure. The intermixing occupancy of *A*-site by La and Sr atoms is evident and extends to about four unit cells. In the nominal LaO plane, only 55% *A*-sites are occupied by La atoms and the other 45% by Sr atoms. The cation intermixing is stronger in the STO capping layer, extending over three unit cells above the nominal LaO plane in comparison to one unit cell below the nominal LaO plane in the substrate. In the same area, intermixing of Ti and Al occurs also in the *B*-type columns. In the BO_2 atomic plane direct above the nominal LaO plane, which is nominally expected to be AlO_2 plane, Al atoms occupy only 35% lattice

sites. In the plane below the nominal LaO plane, which is the TiO_2 terminating plane of the STO substrate, an intermixing of 30% Al with 70% Ti is determined. In the area of cation intermixing, the image intensity values for the oxygen columns show detectable deviation from the substrate area, leading to an oxygen deficiency of about 10%.

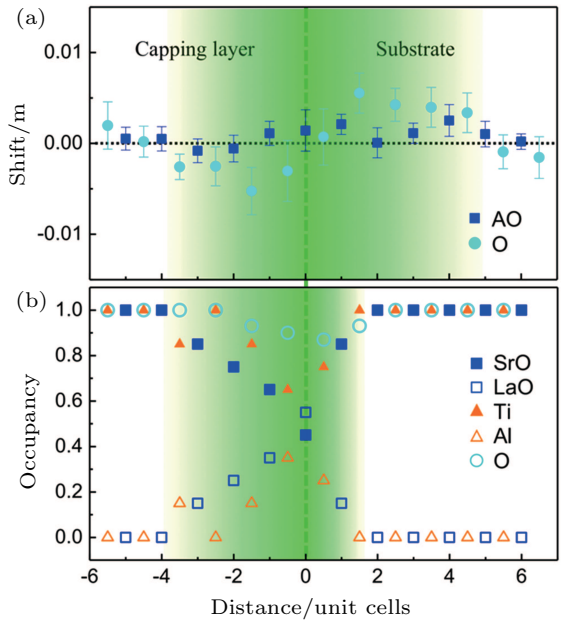


Fig. 15. (color online) (a) The shifts of the *AO*-type columns (SrO and LaO), and of the oxygen columns across the single unit cell layer. (b) Chemical occupancy. The position of the nominal LaO atomic plane is marked by a vertical thick line.[19]

6. NCSI with the C_S/C_C-corrected TEM

In a C_S and C_C (chromatic aberration) corrected electron microscope, such as Jülich PICO 50-300 microscope equipped with an advanced version of C-COR corrector (C-COR+, CEOS GmbH), the two major resolution limitations of the previous instrument generations due to partial spatial and partial temporal coherence are significantly reduced. The C-COR+ corrector allows unwanted coherent axial aberrations of the imaging system to be effectively reduced up to the fourth order, thereby obtaining optimum phase-contrast transfer up to the information limit by adjusting also the fifth-order spherical aberration (C_5).[11]

Under optimum contrast transfer for the NCSI conditions, the instrumental resolution as defined by the information limit is measured using a diffractogram of gold nanoparticles supported by amorphous carbon to be below 50 pm for both 200 and 300 kV TEM and better than 80 pm at 80 kV. However, such measurement has been shown to depend on a number of sample related influences as well as on dynamic and non-linear diffraction effects which may result in an overestimation of the resolving power. Consequently, the concept of object resolution has to be introduced in practical case for the direct perception of resolution by considering the sample-related parameters.

In order to demonstrate the resolving power of the C_S/C_C-corrected PICO microscope, a *b*-axis oriented yttrium-aluminum perovskite (YAP) was selected.[11] At room temperature, YAP has the orthorhombic structure (space group *Pnma*) with lattice parameters $a = 0.5330$ nm, $b = 0.7375$ nm and $c = 0.5180$ nm, as schematically shown in Fig. 16(a). Along the *b*-axis, the Y–Y-atom pairs as marked by the bold lines have projected separations of ~ 57 pm along two directions. The tilts of the corner-shared oxygen octahedra are also indicated by grey rectangles. Figure 16(b) shows an experimental image of YAP without any post filtering. The apparent separations of Y–Y-atom pairs were measured by locally fitting two Gaussian functions to the image intensity distribution. Although they show a variation between 55 pm and 85 pm with a mean value of 69 pm (e.g., see white arrow), the 57 pm separations of the Y–Y-atom pairs are indeed resolved along the two directions as shown by the yellow arrows. To the best of our knowledge, this demonstrates the highest direct resolution in coherent TEM atomic imaging in materials at 200 kV to date. In addition, benefited from the NCSI, the pure O-columns are imaged with very high contrast as outlined by the white lines, which is consistent with the structural model shown in Fig. 16(a).

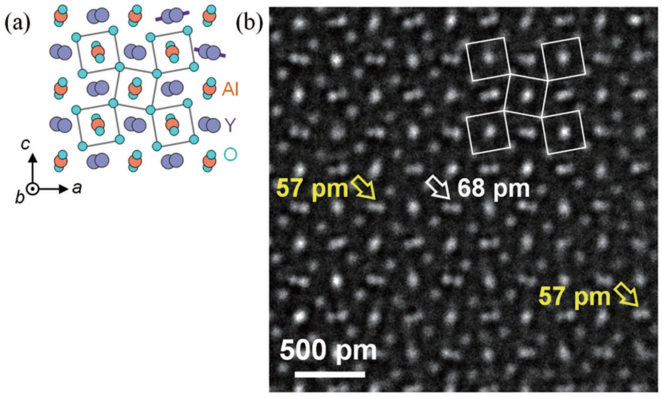


Fig. 16. (color online) (a) Schematic view of $2 \times 2 \times 2$ orthorhombic unit cells along the crystallographic *b* zone axis of YAP. The 57 pm Y–Y-atom pair separation is indicated along two directions by the bold lines. Corners of squares give position of O atoms and centers denote positions of Al overlapping with O atoms. (b) Experimental image of $YAlO_3$:Ce in the [010] projection. Arrows denote examples of Y–Y atom pairs with pair separations given.[11]

It should be emphasized that the resolution improvement by the C_S/C_C correction is of critical importance particularly for the low acceleration voltage. This allows direct visualization of atomic structures in many beam sensitive materials, such as 2D materials (e.g., graphene, metal dichalcogenides, etc) and related structures,[34] although such materials are not the focus of the present review.

7. Summary

We have demonstrated with several examples that structural details, such as the atom positions and chemical occupancy in atomic columns that are parallel to the electron beam, can be obtained from a single HRTEM image. By quantitative comparison of image simulations with the experimental images recorded under the NCSI condition, the atom displacements can be measured with a precision of a few picometers. For ferroelectric materials, based on the precisely determined off-center displacements, the electric dipole of unit cell can be calculated and thus the local polarization can be investigated across the domain walls and lattice defect areas. For some magnetic oxides, local magnetization can also be studied taking the simple relation to the rotation angle of the oxygen octahedra. By quantitative analysis of the image contrast, the intermixing of cations in atomic columns and oxygen deficiency at an interface can be determined. In addition to the above-described examples, another excellent application of the quantitative HRTEM is to determine the three-dimensional shape of a MgO nanocrystal with atomic resolution from a single image. The successful application of the quantitative HRTEM to solving structural problems has played an important role in understanding the relations between structure and properties of materials and is expected to make more progress in the future materials research. On the other hand, based on TEM, other analytical techniques are available, such as electron diffraction, electron holography, scanning TEM imaging and various spectroscopic techniques. Combination of all these techniques provides the optimum capability for insight into the atomic details responsible for the various properties of materials.

Acknowledgment

The authors acknowledge the collaborations with K. Urban, M. Lentzen, A. Thust, J. Barthel, L. Houben, D. Hesse, M. Alexe, I. Vrejoiu, R. Dittmann and F. Gunkel.

References

[1] Setter N and Waser R 2000 *Acta Mater.* **48** 151
[2] Scott J F 2007 *Science* **315** 954
[3] Ohtomo A and Hwang H Y 2004 *Nature* **427** 423
[4] Mannhart J and Schlom D G 2010 *Science* **327** 1607
[5] Nakagawa N, Hwang H Y and Muller D A 2006 *Nat. Mater.* **5** 204
[6] Jia C L, Mi S B, Urban K, Vrejoiu I, Alexe M and Hesse D 2009 *Phys. Rev. Lett.* **102** 117601
[7] Catalan G, Seidel J, Ramesh R and Scott J F 2012 *Rev. Mod. Phys.* **84** 119
[8] Sun Z, Ma C, Liu M, Cui J, Lu L, Lu J, Lou X, Jin L, Wang H and Jia C L 2017 *Adv. Mater.* **29** 1604427
[9] Tang Y L, Zhu Y L, Liu Y, Wang Y J and Ma X L 2017 *Nat. Commun.* **8** 15994
[10] Urban K 2008 *Science* **321** 506
[11] Jin L, Barthel J, Jia C L and Urban K W 2017 *Ultramicroscopy* **176** 99
[12] Jia C L, Mi S B, Barthel J, Wang D W, Dunin-Borkowski R E, Urban K and Thust A 2014 *Nat. Mater.* **13** 1044
[13] Jia C L, Lentzen M and Urban K 2003 *Science* **299** 870
[14] Jia C L, Lentzen M and Urban K 2004 *Microsc. Microanal.* **10** 174
[15] Jia C L, Houben L, Thust A and Barthel J 2010 *Ultramicroscopy* **110** 500
[16] Urban K, Jia C L, Houben L, Lentzen M, Mi S B and Tillmann K 2009 *Phil. Trans. R Soc. A* **367** 3735
[17] Hÿtch M J and Stobbs W M 1994 *Ultramicroscopy* **53** 191
[18] Thust A 2009 *Phys. Rev. Lett.* **102** 220801
[19] Jia C L, Barthel J, Gunkel F, Dittmann R, Hoffmann-Eifert S, Houben L, Lentzen M and Thust A 2013 *Microsc. Microanal.* **19** 310
[20] Kornev I, Fu H and Bellaiche L 2004 *Phys. Rev. Lett.* **93** 196104
[21] Aguado-Puente P and Junquera J 2008 *Phys. Rev. Lett.* **100** 177601
[22] Lubk A, Gemming S and Spaldin N A 2009 *Phys. Rev. B* **80** 104110
[23] Jia C L, Urban K, Alexe M, Hesse D and Vrejoiu I 2011 *Science* **331** 1420
[24] Nelson C T, Winchester B, Zhang Y, Kim S J, Melville A, Adamo C, Folkman C M, Baek S H, Eom C B, Schlom D G, Chen L Q and Pan X 2011 *Nano Lett.* **11** 828
[25] Tang Y L, Zhu Y L, Ma X L, Borisevich A Y, Morozovska A N, Eliseev E A, Wang W Y, Wang Y J, Xu Y B, Zhang Z D and Pennycook S J 2015 *Science* **348** 547
[26] Peters J J P, Apachitei G, Beanland R, Alexe M and Sanchez A M 2016 *Nat. Commun.* **7** 13484
[27] Wei X K, Jia C L, Sluka T, Wang B X, Ye Z G and Setter N 2016 *Nat. Commun.* **7** 12385
[28] Vrejoiu I, Rhun G L, Pintilie L, Hesse D, Alexe M and Gösele U 2006 *Adv. Mater.* **18** 1657
[29] Jia C L, Mi S B, Urban K, Vrejoiu I, Alexe M and Hesse D 2008 *Nat. Mater.* **7** 57
[30] Jia C L, Jin L, Wang D, Mi S B, Alexe M, Hesse D, Reichlova H, Marti X, Bellaiche L and Urban K 2015 *Acta Materialia* **82** 356
[31] Sosnowska I, Schäfer W, Kockelmann W, Andersen K H and Troyanchuk I O 2002 *Appl. Phys. A* **74** S1040
[32] Prokhorenko S, Nahas Y and Bellaiche L 2017 *Phys. Rev. Lett.* **118** 147601
[33] Bellaiche L, Gui Z and Kornev I A 2012 *J. Phys.: Condens. Matter* **24** 312201
[34] Zhang J Y, Zhao D, Xiao D, Ma C, Du H, Li X, Zhang L, Huang J, Huang H, Jia C L, Tománek D and Niu C 2017 *Angew Chem. Int. Ed.* **56** 1850